



A transmission electron microscopy study of EBR-II neutron-irradiated austenitic stainless steel 304 and nickel-base alloy X-750

Xiang Liu ^{a,*}, Lingfeng He ^{a,**}, Huan Yan ^b, Mukesh Bachhav ^a, James F. Stubbins ^b

^a Characterization and Advanced PIE Division, Idaho National Laboratory, Idaho Falls, ID, 83415, USA

^b Department of Nuclear, Plasma, and Radiological Engineering, University of Illinois at Urbana-Champaign, Urbana, IL, 61801, USA

ARTICLE INFO

Article history:

Received 4 May 2019

Received in revised form

15 September 2019

Accepted 13 October 2019

Available online 16 October 2019

Keywords:

Neutron irradiation

Stainless steel

Nickel-base alloys

Frank loops

Transmission electron microscopy (TEM)

Superlattice reflection

ABSTRACT

The microstructure of EBR-II neutron-irradiated austenitic stainless steel 304 and nickel-base alloy X-750 was investigated. Both alloys were irradiated at low dose rates ($\sim 2 \times 10^{-8}$ dpa/s) to a neutron fluence of 6.9×10^{22} n/cm² ($E > 0.1$ MeV) at 371–389 °C. Different types of defects, including Frank loops, cavities, and precipitates were characterized. The Frank loops in Type 304 stainless steel (SS) are larger in size (~ 50 nm in diameter) and lower in number density (2.58×10^{21} m⁻³), compared to most previous higher dose rate neutron irradiation studies. The Frank loops in X-750 have an average size 26.0 nm of and a number density of 9.44×10^{21} m⁻³. In 304 SS and X-750, cavities are of ~ 20 nm and ~ 14 nm in diameter, respectively. The swelling of both alloys was found to be insignificant. In 304 SS, Ni and Si were found enriched at the cavity surfaces and Ni,Si-rich precipitates were also found. Multivariate statistical analysis using non-negative matrix factorization reveals that these Ni,Si-rich precipitates contain only ~ 5.7 at.% Si, differing from the Ni₃Si γ' precipitates found in several previous studies. In X-750, L1₂-structured γ' precipitates were found, and multivariate statistical analysis confirmed the 3:1 stoichiometry (Ni₃(Ti,Al)) of the γ' precipitates and the superlattice reflections confirmed the stability of the crystal structure of these γ' precipitates, indicating higher-than-expected precipitate stability under high-dose neutron irradiation.

© 2019 Elsevier B.V. All rights reserved.

1. Introduction

In 1960s, the EBR-II reactor materials surveillance (SURV) program was initiated to test the performance of fifteen different alloys, including Aluminum Bronze-Ampco Grade 18, Stellite 6B, Inconel X-750, T-1 tool steel, Type 304, 308, 347, 416, 420, 17–4 PH stainless steels (SSs), Beryllium Copper Berylco 25, and Tantalum, under reactor irradiation and thermal aging conditions. Five different types of specimens were tested: tensile test specimens (code T), hardness and corrosion specimens (code V), bend test specimens (code W), impact specimens (code X), coil spring specimens (code Y), and Belleville spring specimens (code Z). Ten subassemblies (SURV-1 to SURV-10) were loaded into EBR-II in 1965. Eight out of the ten subassemblies were irradiated in row 12 of EBR-II to a variety of doses, and two other subassemblies (SURV-6 and

SURV-7) were placed in the primary storage basket and experienced sodium and thermal aging at ~ 370 °C with minimal neutron exposure. The results of SURV-1 [1], SURV-2 [2], SURV-3 [3], SURV-4 and SURV-6 [4], and SURV-5 [5] can be found in previous technical reports. It should be noted that little microstructure information was provided in these reports, which is required to understand the reported property changes after neutron irradiation. This study is the first attempt to investigate the irradiated microstructure of two of the highest-dose SURV specimens, austenitic 304 stainless steel (SS) and nickel-base alloy X-750, utilizing advanced electron microscopy and spectroscopy.

Austenitic stainless steels such as Type 304 SS have broad applications in nuclear reactors. For instance, Type 304 SS is used for core structural and piping in pressurized water reactors (PWRs) [6]. During service, these structural components experience high neutron flux at temperatures close to 300 °C and their microstructure, dimensional stability, phase stability, and mechanical properties can undergo significant changes. The neutron irradiation performance of austenitic SSs have been previously investigated [7–34] and the overall trend of the irradiated microstructure can be

* Corresponding author.

** Corresponding author.

E-mail addresses: Xiang.Liu@inl.gov (X. Liu), Lingfeng.He@inl.gov (L. He).

summarized as: (1) high-density small black-dots and faulted Frank loops at low temperatures; (2) unfaulted loops and network dislocation, voids, and radiation-induced segregation and precipitation at intermediate temperatures; (3) intergranular helium bubbles at high temperatures.

Nickel-base alloy X-750 is a precipitation-hardenable alloy widely used in PWRs and boiling water reactors (BWRs) as core internals [35], and CANDU reactors as spacer material [36]. The degradation of X-750 induced by the combination of stress, reactor irradiation, and temperature can compromise the structural integrity and safety operation of nuclear power plants.

To date, the intergranular stress corrosion cracking (IGSCC) of X-750 has been reported in light water reactors [37]. Embrittlement of X-750 has also been found after irradiation in CANDU reactors. However, little microstructural information was provided in these studies and the irradiated microstructure of X-750 is desired in order to understand the degradation processes from the microstructural level. For instance, the $\text{Ni}_3(\text{Ti},\text{Al})$ (also known as γ') phase with an ordered L1_2 structure is the most important strengthening phase for X-750 but the stability of this phase under neutron irradiation is unknown. A previous in situ 1 MeV Kr^{++} ion irradiation study on X-750 [36] observed disappearing of the superlattice spots, indicating the disordering/dissolution of the ordered γ' precipitates at very low dose (~ 0.06 dpa) at temperatures below 400°C . Most recent studies [38,39] suggested that for X-750 pre-implanted with 5000 appm helium and followed by 40 MeV Ni^+ ion irradiation to 1 dpa at room temperature (RT), γ' were found partially dissolved: superlattice spots disappeared in the diffraction patterns but the chemical composition of the γ' precipitates did not changed significantly (only noticeable change near the peak dose region). However, the γ' superlattice spots were still found for similar irradiation at 400°C , indicating no/little disordering at higher temperatures [38,39]. These ion irradiation studies used different experimental setup (in situ thin foil irradiation vs bulk irradiation with pre-implanted helium), different ions with very different energies (1 MeV Kr^{++} vs 40 MeV Ni^+), and the dose rates are several orders of magnitude higher than actual neutron irradiation. It is thus unclear whether similar disordering/dissolution of the γ' precipitates will happen under neutron irradiation.

Besides the stability of γ' precipitates, other radiation-induced defects, such as dislocation loops and voids, can also have profound impact on the materials properties, e.g. mechanical strength, ductility, dimensional stability, etc. Systematic characterization of the irradiated microstructure is thus desired. In this study, the microstructure of EBR-II neutron-irradiated Type 304 SS and nickel-base alloy X-750 was characterized by transmission electron microscopy (TEM) and scanning transmission electron microscopy with energy dispersive X-ray spectroscopy (STEM-EDS).

2. Experimental

The neutron-irradiated 304 SS and nickel-base alloy X-750 specimens were extracted from the SURV-10 subassembly, and the estimated neutron fluence for both samples was $6.9 \times 10^{22} \text{ n/cm}^2$ ($E > 0.1 \text{ MeV}$). The fluence was equivalent to approximately 24.15 displacement per atom (dpa), and the peak dpa rate of the SURV subassemblies was about $2 \times 10^{-8} \text{ dpa/s}$ [27]. The average irradiation temperature was $371\text{--}389^\circ\text{C}$. During irradiation, the 304 SS specimen was exposed to liquid sodium environment, and the X-750 specimen was exposed to helium environment.

The nominal chemical composition (in wt.%) of 304 SS and X-750 is Fe–18.57Cr–9.46Ni–1.17Mn–0.57Si–0.056C–0.16Mo–0.015P–0.009S–0.013Sn–0.003 Pb, and

Ni–14.7Cr–6.52Fe–2.54Ti–0.78Al–0.94Nb–0.03C–0.55Mn–0.09Cu–0.27Si–0.007S, respectively. The 304 SS was the same material as EBR-II cover plate and was annealed and stress relieved at $468\text{--}496^\circ\text{C}$ for 2 h before irradiation. The X-750 alloy underwent relatively complicate heat treatment [1,27]: the alloy was annealed starting at 427°C and heated to 1149°C at 149°C/h , held at 1149°C for 4 h, followed by air-cooling and rough machining. Then the alloy was age hardened by heating from 427°C to 885°C at 149°C/h , and held at 885°C for 24 h and air cooled. The alloy was finally reheated from 427°C to 704°C at 149°C/h , held at 704°C for 20 h, and air cooled. The final hardness of X-750 is 37–40 Rockwell C.

For post-irradiation examination (PIE), the neutron-irradiated 304 SS and nickel-base alloy X-750 TEM lamellae were prepared using a FEI Quanta 3D FEG DualBeam focused ion beam/scanning electron microscope (FIB/SEM). TEM lamellae were lifted out and thinned to $\sim 100 \text{ nm}$ in thickness using 30 keV Ga ion beam, followed by cleaning with 5 keV and finally 2 keV Ga ion beam. The TEM and STEM-EDS characterization was carried out using a FEI Themis Titan 200 FEG STEM equipped with super-X EDS system and operated at 200 kV. To quantify the defect number density, the average thickness of each TEM lamella was measured by electron energy loss spectroscopy (EELS) in energy-filtered TEM (EFTEM) mode, using a FEI Tecnai TF30-FEG STwin STEM operated at 300 kV. All measured TEM lamella thicknesses are in the range of 120–180 nm.

3. Results and discussions

For 304 SS, the irradiated structure mainly consists of dislocation loops and cavities, similar to those reported in previous neutron irradiation studies on austenitic SSs [12,15,18,20,26]. Fig. 1 shows TEM bright-field (BF) and weak-beam dark-field (WBDF) images of the dislocation loops and several small cavities in irradiated 304 SS. As shown in Fig. 1, when imaged near $[011]$ zone, loops with $(\bar{1}\bar{1}1)$ or $(\bar{1}1\bar{1})$ habit planes appear as edge-on and are perpendicular to $\mathbf{g}_{\bar{1}\bar{1}1}$, and loops with $(11\bar{1})$ or $(\bar{1}\bar{1}1)$ habit planes appear as edge-on and are perpendicular to $\mathbf{g}_{11\bar{1}}$, and loops with (111) , $(\bar{1}11)$, $(1\bar{1}1)$, or $(1\bar{1}\bar{1})$ habit planes appear as elliptical and the major axis direction is perpendicular to \mathbf{g}_{200} . Therefore, it is confirmed the habit plane of these loops are $\{111\}$ planes. In addition, the faulted nature can be seen by the fault contrast [41] in the WBDF image in Fig. 1 (b). Therefore, these loops are Frank faulted loops, which have also been found in previous studies on neutron-irradiated austenitic SSs [12].

In addition to Frank loops and cavities, a significant number of precipitates were found in irradiated X-750, as shown in the STEM high angle annular dark field (HAADF) and BF images at different magnifications in Fig. 2. These precipitates were later confirmed to

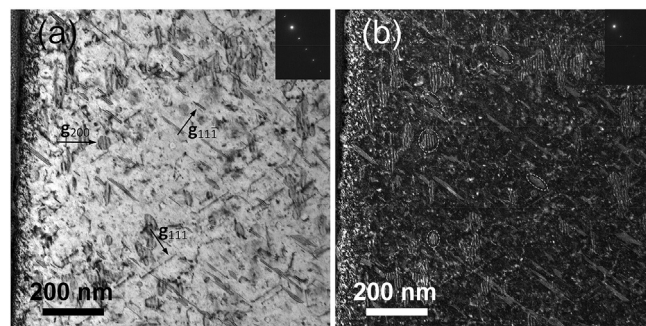


Fig. 1. TEM (a) BF and (b) \mathbf{g}_{5g} WBDF images showing the irradiated microstructure of 304 SS. The images were taken near $[011]$ zone with only $\mathbf{g}_{\bar{1}\bar{1}1}$ strongly excited. The insertions on the top right shows the corresponding diffraction conditions.

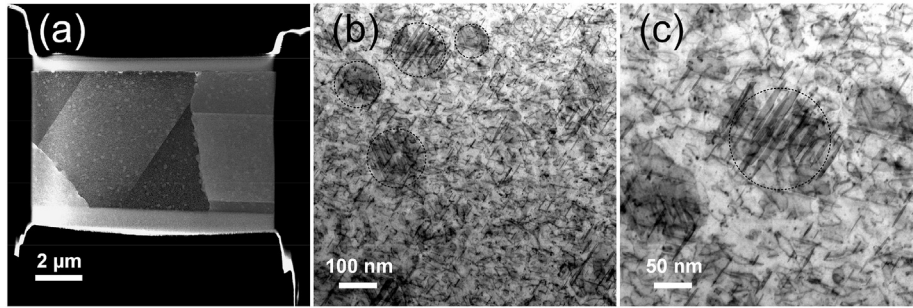


Fig. 2. Overview of X-750 alloy neutron-irradiated to 30.2 dpa at 370 °C: (a) STEM HAADF image showing the precipitates, (b) STEM BF image showing both dislocation loops and precipitates, (c) high-mag STEM BF image showing precipitates are highly decorated by dislocation loops.

be L1₂-structured Ni₃(Ti,Al) γ' precipitates. From the high-mag image in Fig. 2 (c), it is interesting that compared to the matrix, the γ' precipitates contain a higher density of dislocation loops.

3.1. Radiation-induced Frank loops

Rel-rod dark field (DF) is a well-known technique for the characterization of Frank loops in irradiated Face Centered Cubic (FCC) materials [20,24,42]. Fig. 3 (a) and (b) are rel-rod DF images showing Frank loops in irradiated 304 SS on (11 $\bar{1}$) and (1 $\bar{1}$ 1) planes, respectively. The size distribution of the Frank loops is shown by the histogram in Fig. 3 (c). The total number density of Frank loops is estimated to be four times the average density of Frank loops imaged under two different conditions in Fig. 3 (a) and (b), e.g. $\rho_{tot} \cong 2(\rho_{(11\bar{1})} + \rho_{(1\bar{1}1)})$, where ρ_{tot} is the total loop density, $\rho_{(11\bar{1})}$ is the number density of (11 $\bar{1}$) loops and $\rho_{(1\bar{1}1)}$ is the number density of (1 $\bar{1}$ 1) loops. For Frank loops on (11 $\bar{1}$) plane, the measured average size is 48.16 nm with a standard deviation of 29.02 nm, and the density is $5.93 \times 10^{20} \text{ m}^{-3}$. For Frank loops on (1 $\bar{1}$ 1) plane, the measured average size is 52.47 nm with a standard deviation of 28.56 nm, and the density is $7.0 \times 10^{20} \text{ m}^{-3}$. It can be seen that the Frank loops are basically uniformly distributed in each {111} plane. The average size of all measured Frank loops is 50.5 nm and the standard deviation is 28.8 nm, and the average number density is $2.58 \times 10^{21} \text{ m}^{-3}$, based on a measurement of 475 loops. The number density is lower than most reported values from previous SS neutron irradiation studies [16,18,25,30]: for SSs neutron irradiated to high-dose (≥ 10 dpa) in the temperature range of 375 °C–400 °C, previous studies have reported that the Frank loop density to be in the range of $\sim 9 \times 10^{21} \text{ m}^{-3}$ to $3 \times 10^{22} \text{ m}^{-3}$.

For solution annealed Ti-modified austenitic SS JPCA irradiated at 400 °C to 34 dpa in High Flux Isotope Reactor (HFIR) [16], the loop diameter is 12.3 nm and loop concentration is $2.4 \times 10^{22} \text{ m}^{-3}$, the cavity diameter is 2.6 nm and cavity concentration is

$2.9 \times 10^{23} \text{ m}^{-3}$, and corresponding swelling is 0.25%.

In one study [18] on solution annealed (SA) 304 SS, the Frank loop diameter was 7.0 nm and loop density was as high as $7.7 \times 10^{22} \text{ m}^{-3}$ for irradiation in BOR-60 reactor at 330 °C to 40 dpa, and the Frank loop diameter was 12.4 nm and loop density was $3.3 \times 10^{22} \text{ m}^{-3}$ for irradiation in EBR-II reactor at 375 °C to 10 dpa.

In another study [30], 304 SS was irradiated at two different dose rates at similar temperatures: one irradiated to 3.1 dpa at $7.9 \times 10^{-7} \text{ dpa/s}$ at 392 °C and the other one irradiated to 2.6 dpa at $0.8 \times 10^{-7} \text{ dpa/s}$ at 371 °C. It was found that the size of Frank loops was similar, 17.5 nm for the high dose rate one, and 16.0 nm for the low dose rate one. However, the Frank loop density varied by a factor of two: $1.45 \times 10^{22} \text{ m}^{-3}$ for the high dose rate one, and $7.0 \times 10^{21} \text{ m}^{-3}$ for the low dose rate one. The size of voids was also similar (~ 5.0 nm in diameter), but the number density of voids of the high dose rate one was $4 \times 10^{21} \text{ m}^{-3}$, much higher than that of the low dose rate one, which was $7 \times 10^{20} \text{ m}^{-3}$.

It is apparent that compared to previous studies at similar temperatures, the Frank loops we found are about five times larger (50.5 nm vs ~ 10 nm) in size and the number density is only about one fifth to one tenth of the values reported in previous studies ($2.58 \times 10^{21} \text{ m}^{-3}$ vs 7.0×10^{21} – $3.3 \times 10^{22} \text{ m}^{-3}$). The differences should be largely due to the much lower dose rate of the SURV samples. As pointed out in previous study on SURV-5 samples, the peak dose rate of $2 \times 10^{-8} \text{ dpa/s}$ is about one to two orders of magnitude lower than typical accelerated reactor irradiation [27].

Previous studies [43–45] of dose rate effects on the microstructural evolution have found similar dose rate dependence of dislocation loops, e.g. higher loop number density and smaller loop size with increasing dose rate. For high energy electron irradiation, Kiritani [43] predicted a $\phi^{1/2}$ dependence of loop number density, and a $\phi^{-1/2}$ dependence of the loop size, where ϕ is the flux. The dose rate dependence comes from the fact that with increasing dose rate, point defect generation rate increases, which leads to

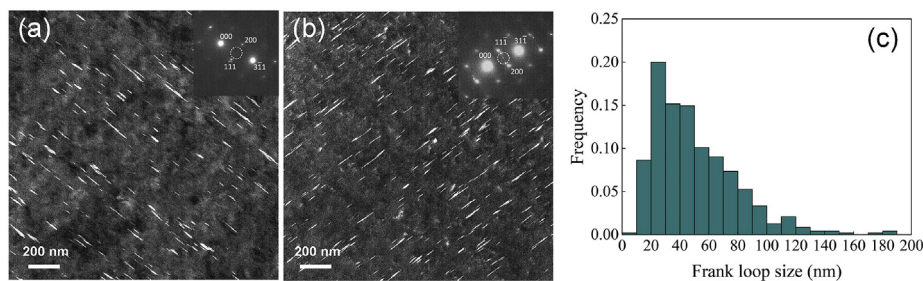


Fig. 3. TEM rel-rod DF images showing the Frank loops in irradiated 304 SS imaged near [011] zone: (a) only direct beam and g_{111}^- are strongly excited, and (b) only direct beam and g_{111}^+ are strongly excited. The insertions on the top right shows the corresponding diffraction conditions. The dotted circles indicate the location of objective aperture. (c) is the histogram of the size distribution of Frank loops based on the measurement of loops in Fig. 3 (a) and (b).

enhanced defect mutual recombination and consequently suppressed loop growth [45]. The importance of mutual recombination implies that the system is in the recombination-dominant regime, which is consistent with the observed relatively low density of defect sinks in 304 SS, and is also consistent with previous findings [45] that recombination regime covers $\sim 400^\circ\text{C}$ irradiations for austenitic SSs.

Similar rel-rod DF imaging technique was used to characterize the Frank loops in irradiated X-750. Fig. 4 (a) and (b) shows the Frank loops on $(11\bar{1})$ and $(1\bar{1}1)$ planes, respectively. Again, the Frank loop distribution on $(11\bar{1})$ and $(1\bar{1}1)$ planes were found to be similar. The corresponding loop size distribution histogram is shown in Fig. 4 (c). Compared to 304 SS, the Frank loops in X-750 are much smaller, with an average size of 26.0 nm and a standard deviation of 12.4 nm, and the average number density is $9.44 \times 10^{21} \text{ m}^{-3}$, based on a measurement of 289 loops.

3.2. Radiation-induced cavities

The radiation-induced cavities in irradiated 304 SS were found uniformly distributed in the matrix, as shown in the STEM BF and HAADF images in Fig. 5 (a) and (b), together with the size distribution histogram in Fig. 5 (c). Based on a measurement of 97 cavities, the average cavity size is $19.2 \pm 4.0 \text{ nm}$ (diameter) and the number density is $2.87 \times 10^{20} \text{ m}^{-3}$. The corresponding swelling is only 0.11%. The previous study [27] on lower dose SURV 304 SS reported very slightly ($\sim 0.38\%$) drop in density. Considering the uncertainty of density measurements, comparison of SURV-5 (neutron fluence $3.2 \times 10^{22} \text{ n/cm}^2$) and SURV-10 (neutron fluence $6.9 \times 10^{22} \text{ n/cm}^2$) results show no accelerated swelling happened. There are two possible reasons for observed low swelling: one is that the swelling of 304 SS is still in the early transient regime, and the other one is that the system in a recently found steady-state swelling regime with a swelling rate of only $\sim 0.07\%/ \text{dpa}$ [13]. This low rate steady-state swelling regime is expected under low temperate and low dose rate irradiation conditions.

STEM-EDS mapping was used to investigate the elemental distribution. Fig. 6 shows the STEM-BF image together with corresponding elemental maps. It is clear that the cavity-matrix interface is enriched in Ni, and depleted in Fe and Cr. Fig. 6 (d) also clearly shows that Ni is enriched at the dislocation loops. Although Si and Mn counts are relatively low, it can still be seen that Si follows similar enrichment behavior as Ni, and Mn follows similar depletion behavior as Fe and Cr. The enrichment of Ni at a dislocation loop and a void is quantitatively shown in the line scans in Fig. 6 (g) and Fig. 6 (h), respectively. In Fig. 6 (g), Ni enriched by $\sim 6.9 \text{ at.}\%$ at the dislocation loop. In Fig. 6 (h), Ni enriched by $\sim 7.9 \text{ at.}\%$ and $\sim 5.1 \text{ at.}\%$ at the two void-matrix interfaces.

In addition to Ni and Si enrichment at cavity-matrix interfaces

and dislocation loops, some Ni,Si-rich particles are also found in the EDS maps in Fig. 6, although they are almost invisible in STEM BF images. In order to better quantify the composition of the Ni,Si-rich precipitates, multivariate statistical analysis (MVSA) using non-negative matrix factorization (NMF) method in multi-dimensional data analysis toolkit HyperSpy was employed [46]. The results before and after NMF are shown in Fig. 7. The NMF method successfully separated out the Ni,Si-rich phase, as demonstrated by the EDS spectra in Fig. 7 (f). It is easy to see that the Ni,Si-rich phase basically only contains Ni and Si. Based on NMF and Cliff-Lorimer (C-L) quantification method, the Ni,Si-rich phase has a Si concentration of about 5.7 at.%. These Ni,Si-rich particles are somewhat different from the Ni_3Si (also known as γ') phase found in neutron-irradiated 316 SS and its variants in several previous studies [8,12,20,22,26,32], and no superlattice reflections were found.

The necessity of MVSA can be quickly appreciated by the results in Fig. 7. The line scan over a Ni,Si-rich precipitate in Fig. 7 (g) is based on the collected raw EDS spectrum before NMF. The region between ~ 62 and $\sim 98 \text{ nm}$ is the Ni,Si-rich precipitate. It can be seen that at the center of the precipitate, the peak Ni and Si concentration is about 18.0 at.% and 0.8 at.%. In contrast, the results after MVSA clearly shows the precipitate basically only contains Ni ($\sim 94 \text{ at.}\%$) and Si ($\sim 5.7 \text{ at.}\%$). Without MVSA, significant amount of signal from the matrix compromises the quantitative EDS analysis and one would incorrectly think that the precipitate still contains significant amount of Fe and Cr.

Compared to irradiated 304 SS, the cavities in irradiated X-750 are much smaller in size and lower in number density. Different from the multifaceted cavities in 304 SS, the ones in X-750 are basically of globular shape, which could be due to their small size. Fig. 8 (a) and (b) are the STEM BF and HAADF image showing the cavities in irradiated X-750, together with the size distribution histogram in Fig. 8 (c). Based on the measurement of 76 cavities, the average cavity size is $14.5 \pm 4.5 \text{ nm}$ (diameter), and the average number density is $2.74 \times 10^{19} \text{ m}^{-3}$.

Little data on the swelling of X-750 under neutron irradiation is currently available. An early work on X-750 neutron-irradiated to $\sim 0.4 \text{ dpa}$ reported some 1.5–8 nm cavities in the matrix, but the number density was not reported [47]. Based on the cavity size and number density, the swelling of irradiated X-750 investigated in current study is merely 0.0044%. Previous study on lower dose SURV X-750 samples reported no swelling at a neutron fluence of $3.2 \times 10^{22} \text{ n/cm}^2$ [27]. Together, X-750 shows exceptional swelling resistance.

It is known that the helium atoms can be produced from the two-step transmutation reaction of nickel: $^{58}\text{Ni}(n,\gamma)^{59}\text{Ni}(n,\alpha)^{56}\text{Fe}$ [17,48]. The helium content in irradiated 304 SS and X-750 can be estimated based on the EBR-II neutron spectrum. The average He/dpa ratio is about $\sim 0.25 \text{ appm/dpa}$ for 304 SS in the EBR-II reflector

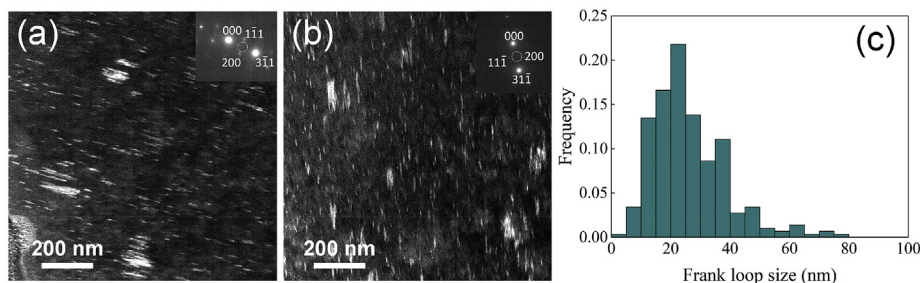


Fig. 4. TEM rel-rod DF images showing the Frank loops in irradiated X-750 imaged near $[011]$ zone: (a) only direct beam and g_{311} are strongly excited, and (b) only direct beam and g_{311} are strongly excited. The insertions on the top right shows the corresponding diffraction conditions. The dotted circles indicate the location of objective aperture. (c) is the histogram of the size distribution of Frank loops.

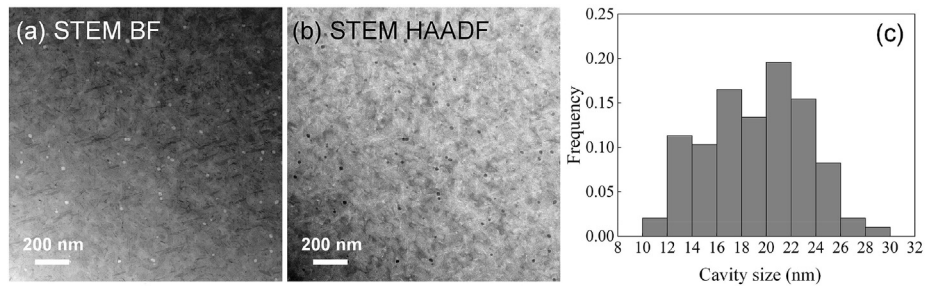


Fig. 5. (a) STEM BF image, (b) STEM HAADF image showing the cavities, and (c) size distribution histogram of the cavities in irradiated 304 SS.

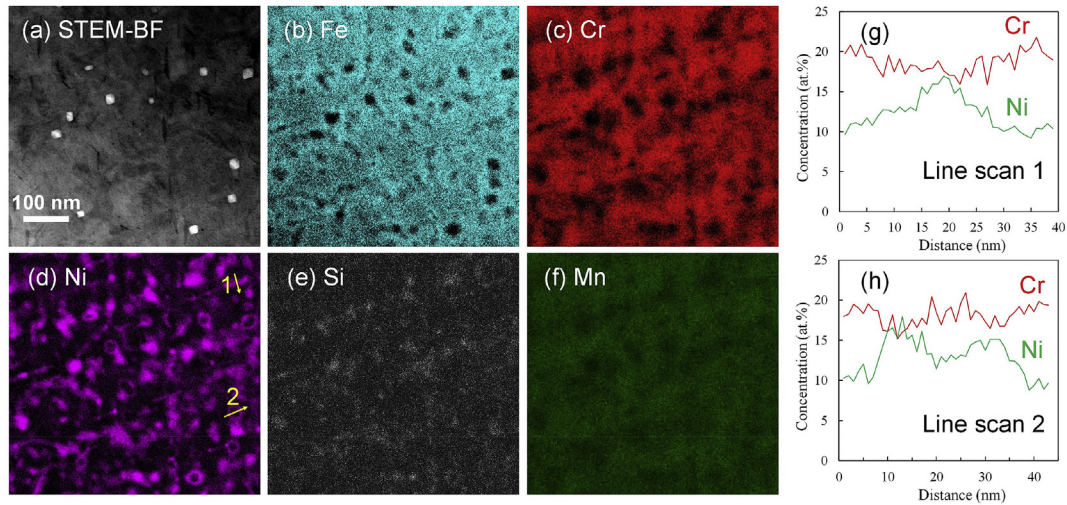


Fig. 6. STEM-EDS mapping results of irradiated 304 SS: (a) STEM BF and the elemental distribution of (b) Fe, (c) Cr, (d) Ni, (e) Si, (f) Mn, (g) line scan across a dislocation loop highlighted in (d), and (h) line scan across a void highlighted in (d).

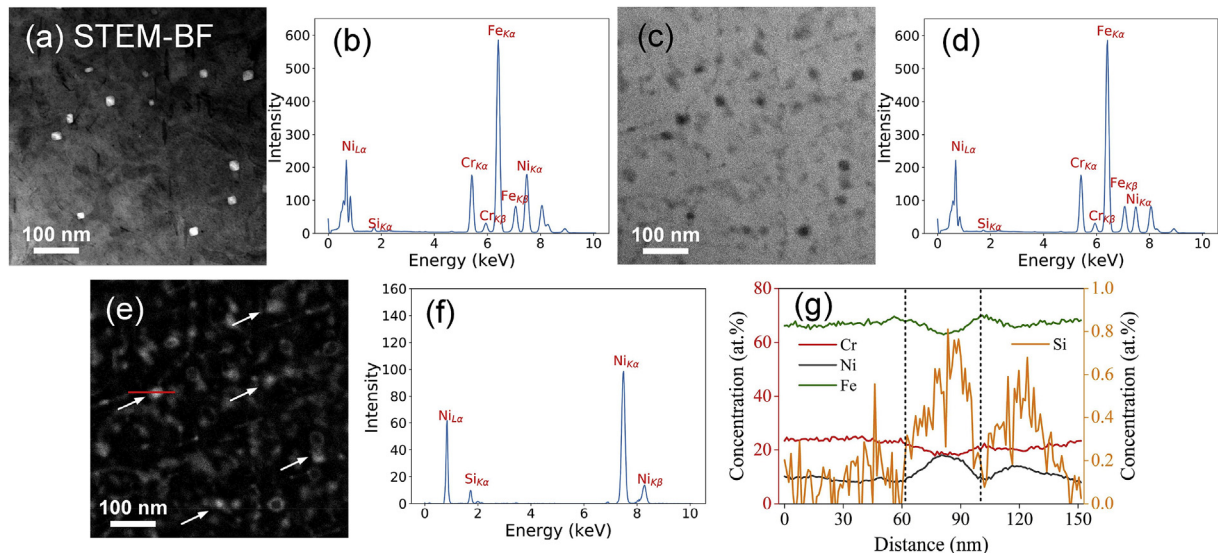


Fig. 7. MVSA using NMF of the STEM-EDS data for 304 SS: (a) STEM-BF image, (b) raw EDS spectrum, (c) distribution of matrix phase after NMF, (d) separated EDS spectrum of the matrix phase after NMF, (e) distribution of Ni,Si-rich phase after NMF, with several Ni,Si-rich precipitates marked by arrows, (f) separated EDS spectrum of the Ni,Si-rich phase after NMF, and (g) EDS line scan showing the elemental concentration across the precipitate marked by red solid line in (e). (For interpretation of the references to colour in this figure legend, the reader is referred to the Web version of this article.)

[17], and this number should be a good approximation for 304 SS in row 12. The estimated helium levels in 304 SS and X-750 are ~6.0 appm, and ~47.0 appm, respectively. Assuming all the helium atoms

are only present in the cavities and the average distance between helium atoms is comparable to the lattice constant of the matrix, the swelling would be on the order of 0.0006%, which is way below

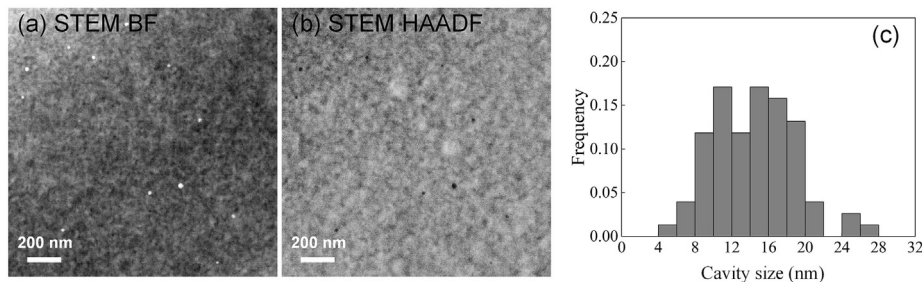


Fig. 8. (a) STEM BF image, (b) STEM HAADF image showing the cavities, and (c) size distribution histogram of the cavities in irradiated X-750.

measured 0.11% swelling. Therefore, the cavities in 304 SS should be voids. Under similar assumption, the swelling of X-750 would be on the order of 0.0047%, which is close to the measured swelling of 0.0044%. Therefore, the cavities in X-750 could be helium-filled cavities.

3.3. γ' precipitates In irradiated X-750

As mentioned previously, a significant number of precipitates were found in irradiated X-750. These precipitates were further characterized using STEM-EDS. As shown in the HAADF image in Fig. 9 (a) and element maps in Fig. 9 (b)–(h), these precipitates are enriched in Ni, Ti, and Al, which is consistent with the $\text{Ni}_3(\text{Ti},\text{Al})$ γ' precipitates commonly found in nickel-base alloys. As shown in Fig. 11, TEM diffraction patterns were used to confirm that these precipitates are indeed γ' precipitates. Fig. 9 also shows that coarse γ' precipitates were found at high-angle grain boundaries (HAGBs), but not at $\Sigma 3$ twin boundaries. Several coarse precipitates at HAGBs also contain Nb.

In order to confirm the 3:1 stoichiometry of the $\text{Ni}_3(\text{Ti},\text{Al})$ γ' precipitates in X-750, similar MVSA using NMF was carried out. The results are shown in Fig. 10, in which there are three phases: the matrix, the Cr-rich carbide phase at grain boundary, and the Ti,Al-rich phase. The EDS spectrum of the Cr-rich carbide and the Ti,Al-rich precipitates were successfully separated using the NMF method, as demonstrated in Fig. 10 (f) and (g).

Based on the spectrum obtained from NMF and C-L quantification method, it was found that the measured composition of the Ti,Al-rich precipitates is about 74.7 at.% Ni, 22.9 at.% Ti, and 2.3 at.% Al. The Ni: (Ti + Al) ratio is very close to 3, indicating that these precipitates are indeed $\text{Ni}_3(\text{Ti},\text{Al})$, and their Ti content is much higher than Al content.

A previous ion irradiation study [36] has shown that the superlattice reflections of γ' precipitates in X-750 disappeared after

in situ heavy ion irradiation to very low doses at temperatures below 400 °C, indicating that γ' precipitates underwent disordering/dissolution. Fig. 11 shows the TEM diffraction patterns of γ' precipitates in different grains at different orientations. It was found that, although very weak, the superlattice reflections are still present in all cases, indicating that the γ' precipitates in X-750 have not undergone significant disordering, even after high dose (~24.15 dpa) fast neutron irradiation at relatively low temperature (~371–389 °C). Our results show that under low dose rate neutron irradiation at 371–389 °C, the radiation-enhanced back diffusion is strong enough to compete with ballistic mixing caused by cascade damage, leading to relatively stable $\text{Ni}_3(\text{Ti},\text{Al})$ γ' precipitates in X-750. However, the much lower Ni and Si content in 304 SS makes it more difficult to form and maintain silicon levels of Ni,Si-rich precipitates against ballistic mixing.

The SURV program started too long time ago and due to the unavailability of the archive X-750 samples, the original size of the γ' precipitates is unknown. Therefore, it is not clear whether these γ' precipitates found in irradiated X-750 are bigger or smaller than the unirradiated ones. As predicted by previous modeling studies [49–51] on the stability of precipitates, the equilibrium size (if exists) of precipitates under irradiation is determined by the competition of ballistic mixing and radiation-enhanced back diffusion, and could be either bigger or smaller than the original size. In addition, although these γ' precipitates have not been dissolved by neutron irradiation and the basic crystal structure was unchanged, it was found that the γ' precipitates contains significant amount of dislocation loops, as shown in Fig. 2.

4. Conclusions

Examination of the irradiation performance of legacy specimens generated from past irradiation programs using state-of-the-art characterization techniques can provide critical data and help

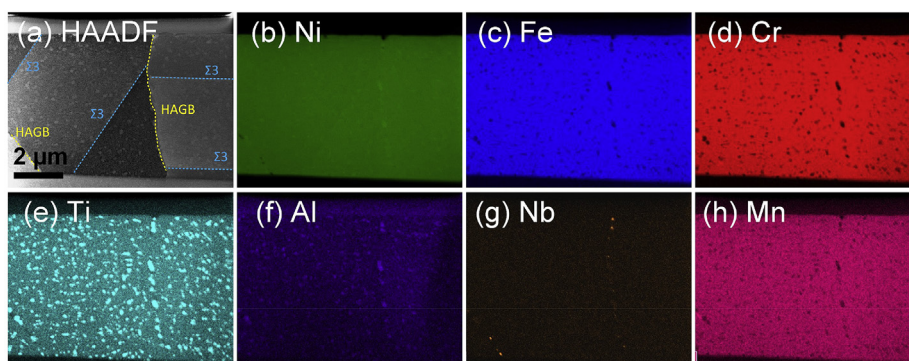


Fig. 9. STEM-EDS mapping results showing (a) STEM HAADF image and elemental distribution of (b) Ni, (c) Fe, (d) Cr, (e) Ti, (f) Al, (g) Nb, and (h) Mn in irradiated X-750.

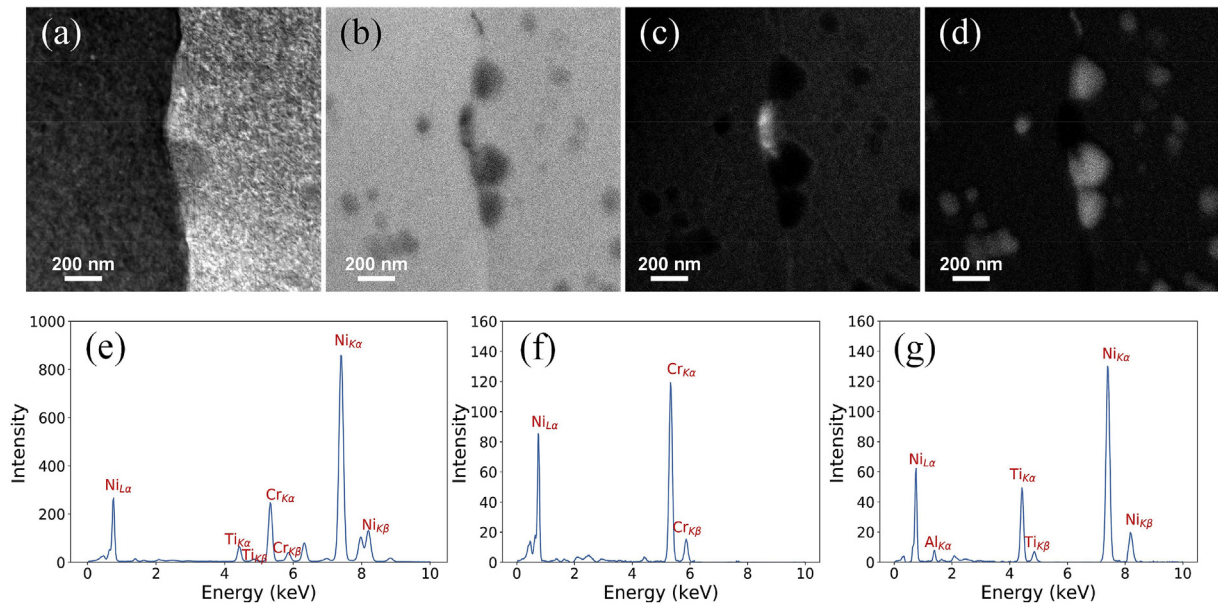


Fig. 10. MVSA using NMF of the STEM-EDS data for X-750: (a) STEM-BF image, (b) distribution of matrix phase after NMF, (c) Cr-rich phase after NMF, (d) Ti,Al-rich phase after NMF, (e) raw EDS spectrum of before NMF, (f) separated EDS spectrum of the Cr-rich phase after NMF, and (g) separated EDS spectrum of the Ti,Al-rich phase after NMF.

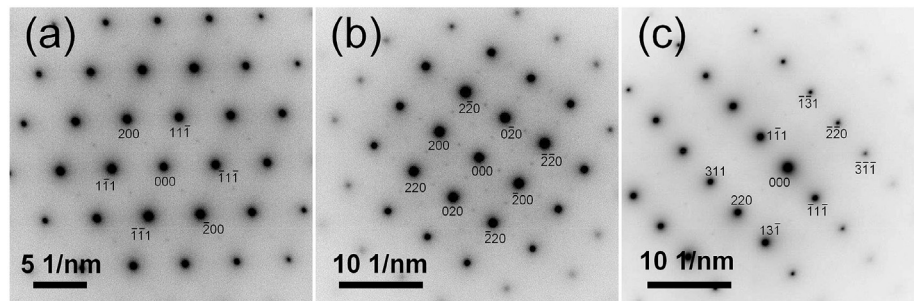


Fig. 11. TEM diffraction patterns showing the superlattice diffractions from the γ' precipitates in irradiated X-750 in different grains on three different zones: (a) [011] zone, (b) [001] zone, and (c) [112] zone.

address the materials challenges facing the development of advanced fast reactors. This study investigated two reactor structural materials, 304 SS and nickel-base alloy X-750, from the highest dose (SURV-10) of the EBR-II SURV program that initiated in 1960s. After being irradiated in the EBR-II reactor at low dose rates ($\sim 2 \times 10^{-8}$ dpa/s) to 24.15 dpa at ~ 371 – 389 °C, a series of microstructural modifications in 304 SS and nickel base alloy X-750 were identified and characterized:

1. Dislocation loops. The dislocation structure was found to be dominated by Frank faulted loops in both 304 SS and X-750. For 304 SS, a strong dose rate effect was observed: the Frank loops after long-term low dose rate neutron irradiation are much larger in size and much smaller in number density, compared to previous higher dose rate neutron irradiation results.
2. Cavities. Even though cavities are commonly found in both 304 SS and X-750, the overall swelling of both alloys is minimal (0.11% in 304 SS and 0.0044% in X-750). An estimation of the helium content in 304 SS and X-750 indicate the cavities in 304 SS are voids, whereas the cavities in X-750 could be helium bubbles.
3. Precipitates. In 304 SS, apparent enrichment of Ni and Si was found at the cavity surfaces. In addition, Ni,Si-rich precipitates

with a Si content of ~ 5.7 at.% (after non-negative matrix factorization) were also found in 304 SS. In X-750, significant amount of $\text{Ni}_3(\text{Ti,Al})$ γ' precipitates were identified using STEM-EDS and TEM diffraction. The 3:1 stoichiometry was confirmed using non-negative matrix factorization and Cliff-Lorimer quantification. In contrast to previous studies on X-750 that found dissolution of γ' precipitates under even low dose ion irradiation, current findings indicate that under neutron irradiation, these γ' precipitates are more stable than expected. The difference could be due to low dose rate of neutron irradiation.

Data availability

The raw/processed data required to reproduce these findings cannot be shared at this time as the data also forms part of an ongoing study.

Declaration of competing interest

The authors declare that they have no known competing financial interests or personal relationships that could have appeared to influence the work reported in this paper.

Acknowledgments

This manuscript has been authored by Battelle Energy Alliance, LLC under Contract No. DE-AC07-05ID14517 with the U.S. Department of Energy. The U. S. Government retains and the publisher, by accepting the article for publication, acknowledges that the U. S. Government retains a nonexclusive, paid-up, irrevocable, worldwide license to publish or reproduce the published form of this manuscript, or allow others to do so, for U. S. Government purposes. The authors would like to thank Douglas L. Porter for his helpful information on the SURV samples. The authors would like to thank Collin Knight, Alexander J. Winston, Alex N. Pomo, Nickolas M. Bolender, Mark D. Taylor, Jason P. Bush, Jeffery D. Bailey, Daniel J. Murray, Brandon J. Hernandez, and Miles T. Cook for their help and support on this project. This work was funded by the Laboratory Directed Research and Development program (LDRD project #18A12-150FP) at Idaho National Laboratory. X. Liu and L. He also acknowledges the financial support from U.S. Department of Energy, Office of Nuclear Energy under DOE Idaho Operations Office Contract DEAC07-05ID14517 as part of a Nuclear Science User Facilities.

References

- [1] S. Greenberg, The EBR-II Materials-Surveillance Program: I. Program And Results of SURV-1, 1969.
- [2] S. Greenberg, R.V. Strain, The EBR-II Materials-Surveillance Program: II. Results of SURV-2, 1970.
- [3] S. Greenberg, R.V. Strain, E.R. Ebersole, The EBR-II Materials-Surveillance Program: III. Results of SURV-3, 1972.
- [4] W.E. Ruther, G.O. Hayner, B.G. Carlson, E.R. Ebersole, T.R. Allen, The EBR-II Materials-Surveillance Program: IV. Results of SURV-4 and SURV-6, 1998.
- [5] W.E. Ruther, J.D. Staffon, B.G. Carlson, T.R. Allen, The EBR-II Materials-Surveillance Program: V. Results of SURV-5, 1998.
- [6] S.J. Zinkle, G.S. Was, Materials challenges in nuclear energy, *Acta Mater.* 61 (2013) 735–758, <https://doi.org/10.1016/j.actamat.2012.11.004>.
- [7] A. Etienne, B. Radiguet, P. Pareige, J.-P. Massoud, C. Pokor, Tomographic atom probe characterization of the microstructure of a cold worked 316 austenitic stainless steel after neutron irradiation, *J. Nucl. Mater.* 382 (2008) 64–69, <https://doi.org/10.1016/j.jnucmat.2008.09.015>.
- [8] C. Cawthorne, C. Brown, The occurrence of an ordered FCC phase in neutron irradiated M316 stainless steel, *J. Nucl. Mater.* 66 (1977) 201–202, [https://doi.org/10.1016/0022-3115\(77\)90149-0](https://doi.org/10.1016/0022-3115(77)90149-0).
- [9] E.E. Bloom, J.O. Stiegler, C.J. McHargue, Radiation damage in annealed type 304 stainless steel, *Radiat. Eff.* 14 (1972) 231–243, <https://doi.org/10.1080/00337577208231205>.
- [10] Y. Chen, P.H. Chou, E.A. Marquis, Quantitative atom probe tomography characterization of microstructures in a proton irradiated 304 stainless steel, *J. Nucl. Mater.* 451 (2014) 130–136, <https://doi.org/10.1016/j.jnucmat.2014.03.034>.
- [11] Y. Ishiyama, M. Kodama, N. Yokota, K. Asano, T. Kato, K. Fukuya, Post-irradiation annealing effects on microstructure and helium bubbles in neutron irradiated type 304 stainless steel, *J. Nucl. Mater.* 239 (1996) 90–94, [https://doi.org/10.1016/S0022-3115\(96\)00465-5](https://doi.org/10.1016/S0022-3115(96)00465-5).
- [12] P.J. Maziasz, Overview of microstructural evolution in neutron-irradiated austenitic stainless steels, *J. Nucl. Mater.* 205 (1993) 118–145, [https://doi.org/10.1016/0022-3115\(93\)90077-C](https://doi.org/10.1016/0022-3115(93)90077-C).
- [13] F.A. Garner, New data and insights on prediction of void swelling in austenitic pressure vessel internals, in: *Fontevraud 9*, Avignon, France, 2018.
- [14] B.H. Sencer, G.M. Bond, M.L. Hamilton, F.A. Garner, S.A. Maloy, W.F. Sommer, Microstructural origins of radiation-induced changes in mechanical properties of 316 L and 304 L austenitic stainless steels irradiated with mixed spectra of high-energy protons and spallation neutrons, *J. Nucl. Mater.* (2001) 112–118, [https://doi.org/10.1016/S0022-3115\(01\)00512-8](https://doi.org/10.1016/S0022-3115(01)00512-8).
- [15] L. Tan, R.E. Stoller, K.G. Field, Y. Yang, H. Nam, D. Morgan, B.D. Wirth, M.N. Gussev, J.T. Busby, Microstructural evolution of type 304 and 316 stainless steels under neutron irradiation at LWR relevant conditions, *JOM* 68 (2016) 517–529, <https://doi.org/10.1007/s11837-015-1753-5>.
- [16] M.P. Tanaka, S. Hamada, A. Hishinuma, P.J. Maziasz, Microstructural development of austenitic stainless steels irradiated in HFIR, *J. Nucl. Mater.* 155–157 (1988) 801–805, [https://doi.org/10.1016/0022-3115\(88\)90419-9](https://doi.org/10.1016/0022-3115(88)90419-9).
- [17] F.A. Garner, B.M. Oliver, L.R. Greenwood, D.L. Porter, T. Allen, D.W. Vehar, D.M. Gilliam, J.M. Adams, S.W. Dean, Measurement of helium generation in AISI 304 reflector and blanket assemblies after long-term irradiation in EBR-II, *J. ASTM Int. (JAI)* 4 (2007) 100342, <https://doi.org/10.1520/JAI100342>.
- [18] C. Pokor, Y. Brechet, P. Dubuisson, J.P. Massoud, A. Barbu, Irradiation damage in 304 and 316 stainless steels: experimental investigation and modeling. Part I: evolution of the microstructure, *J. Nucl. Mater.* 326 (2004) 19–29, <https://doi.org/10.1016/j.jnucmat.2003.11.007>.
- [19] J.O. Stiegler, E.E. Bloom, The effects of large fast-neutron fluences on the structure of stainless steel, *J. Nucl. Mater.* 33 (1969) 173–185, [https://doi.org/10.1016/0022-3115\(69\)90058-0](https://doi.org/10.1016/0022-3115(69)90058-0).
- [20] D.J. Edwards, E.P. Simonen, F.A. Garner, L.R. Greenwood, B.M. Oliver, S.M. Bruemmer, Influence of irradiation temperature and dose gradients on the microstructural evolution in neutron-irradiated 316 SS, *J. Nucl. Mater.* 317 (2003) 32–45, [https://doi.org/10.1016/S0022-3115\(03\)00003-5](https://doi.org/10.1016/S0022-3115(03)00003-5).
- [21] T. Toyama, Y. Nozawa, W. Van Renterghem, Y. Matsukawa, M. Hatakeyama, Y. Nagai, A. Al Mazouzi, S. Van Dyck, Grain boundary segregation in neutron-irradiated 304 stainless steel studied by atom probe tomography, *J. Nucl. Mater.* 425 (2012) 71–75, <https://doi.org/10.1016/j.jnucmat.2011.11.072>.
- [22] P.J. Maziasz, Formation and stability of radiation-induced phases in neutron-irradiated austenitic and ferritic steels, *J. Nucl. Mater.* 169 (1989) 95–115, [https://doi.org/10.1016/0022-3115\(89\)90525-4](https://doi.org/10.1016/0022-3115(89)90525-4).
- [23] R. Carlander, S.D. Harkness, F.L. Yaggee, Fast-neutron effects on type-304 stainless steel, *Nucl. Appl. Technol.* 7 (1969) 67–75, <https://doi.org/10.13182/NT69-A28387>.
- [24] D.J. Edwards, E.P. Simonen, S.M. Bruemmer, Evolution of fine-scale defects in stainless steels neutron-irradiated at 275 °C, *J. Nucl. Mater.* 317 (2003) 13–31, [https://doi.org/10.1016/S0022-3115\(03\)00002-3](https://doi.org/10.1016/S0022-3115(03)00002-3).
- [25] S.J. Zinkle, P.J. Maziasz, R.E. Stoller, Dose dependence of the microstructural evolution in neutron-irradiated austenitic stainless steel, *J. Nucl. Mater.* 206 (1993) 266–286, [https://doi.org/10.1016/0022-3115\(93\)90128-L](https://doi.org/10.1016/0022-3115(93)90128-L).
- [26] H.R. Brager, F.A. Garner, Dependence of Void Formation on Phase Stability in Neutron-Irradiated Type 316 Stainless Steel, in: *Eff. Radiat. Struct. Mater.*, ASTM International, 100 Barr Harbor Drive, PO Box C700, West Conshohocken, PA 19428-2959, n.d.: pp. 207–207–26. doi:10.1520/STP381675
- [27] T.R. Allen, C.L. Trybus, J.I. Cole, Effects of low dose rate irradiation and thermal aging on reactor structural alloys, *J. Nucl. Mater.* 270 (1999) 290–300, [https://doi.org/10.1016/S0022-3115\(99\)00010-0](https://doi.org/10.1016/S0022-3115(99)00010-0).
- [28] W. Karlens, S. Van Dyck, The effect of prior cold-work on the deformation behaviour of neutron irradiated AISI 304 austenitic stainless steel, *J. Nucl. Mater.* 406 (2010) 127–137, <https://doi.org/10.1016/j.jnucmat.2010.01.028>.
- [29] T.R. Allen, J.I. Cole, C.L. Trybus, D.L. Porter, H. Tsai, F. Garner, E.A. Kenik, T. Yoshitake, J. Ohta, The effect of dose rate on the response of austenitic stainless steels to neutron radiation, *J. Nucl. Mater.* 348 (2006) 148–164, <https://doi.org/10.1016/j.jnucmat.2005.09.011>.
- [30] H.R. Brager, L.D. Blackburn, D.L. Greenslade, The dependence on displacement rate of radiation-induced changes in microstructure and tensile properties of AISI 304 and 316, *J. Nucl. Mater.* 122 (1984) 332–337, [https://doi.org/10.1016/0022-3115\(84\)90620-2](https://doi.org/10.1016/0022-3115(84)90620-2).
- [31] A. Renault, J. Malaplate, C. Pokor, P. Gavoille, TEM and EFTEM characterization of solution annealed 304L stainless steel irradiated in PHENIX, up to 36 dpa and at 390 °C, *J. Nucl. Mater.* 421 (2012) 124–131, <https://doi.org/10.1016/j.jnucmat.2011.10.049>.
- [32] H.R. Brager, F.A. Garner, Swelling as a consequence of gamma prime (γ') and M23(C, Si)₆ formation in neutron irradiated 316 stainless steel, *J. Nucl. Mater.* 73 (1978) 9–19, [https://doi.org/10.1016/0022-3115\(78\)90474-9](https://doi.org/10.1016/0022-3115(78)90474-9).
- [33] F.A. Garner, E.P. Simonen, B.M. Oliver, L.R. Greenwood, M.L. Grossbeck, W.G. Wolfer, P.M. Scott, Retention of hydrogen in fcc metals irradiated at temperatures leading to high densities of bubbles or voids, *J. Nucl. Mater.* 356 (2006) 122–135, <https://doi.org/10.1016/j.jnucmat.2006.05.023>.
- [34] E.A. Kenik, Radiation-induced segregation in irradiated Type 304 stainless steels, *J. Nucl. Mater.* 187 (1992) 239–246, [https://doi.org/10.1016/0022-3115\(92\)90503-D](https://doi.org/10.1016/0022-3115(92)90503-D).
- [35] L.C. Walters, W.E. Ruther, In-reactor stress relaxation of Inconel X750 springs, *J. Nucl. Mater.* 68 (1977) 324–333, [https://doi.org/10.1016/0022-3115\(77\)90257-4](https://doi.org/10.1016/0022-3115(77)90257-4).
- [36] H.K. Zhang, Z. Yao, C. Judge, M. Griffiths, Microstructural evolution of CANDU spacer material Inconel X-750 under in situ ion irradiation, *J. Nucl. Mater.* 443 (2013) 49–58, <https://doi.org/10.1016/j.jnucmat.2013.06.034>.
- [37] H. Hänninen, I. Aho-Mantila, K. Törrönen, *Environment Sensitive Cracking in Pressure Boundary Materials of Light Water Reactors*, 1987.
- [38] P. Changizian, Z. Yao, C. Lu, F. Long, M.R. Daymond, Radiation effect on nano-indentation properties and deformation mechanism of a Ni-based superalloy X-750, *J. Nucl. Mater.* (2018), <https://doi.org/10.1016/j.jnucmat.2018.11.040>.
- [39] P. Changizian, A. Brooks, Z. Yao, M.R. Daymond, Nano-scale mechanical properties and microstructure of irradiated X-750 Ni-based superalloy, *Metall. Mater. Trans. A* 49 (2018) 498–514, <https://doi.org/10.1007/s11661-017-4445-7>.
- [40] W.-Y. Chen, J. Wen, M.A. Kirk, Y. Miao, B. Ye, B.R. Kleinfieldt, A.J. Oaks, J.F. Stubbins, Characterization of dislocation loops in CeO₂ irradiated with high energy Krypton and Xenon, *Philos. Mag.* 93 (2013) 4569–4581, <https://doi.org/10.1080/14786435.2013.838007>.
- [41] C. Xu, W.-Y. Chen, Y. Chen, Y. Yang, Microstructural evolution of NF709 austenitic stainless steel under in-situ ion irradiations at room temperature, 300, 400, 500 and 600 °C, *J. Nucl. Mater.* 509 (2018) 644–653, <https://doi.org/10.1016/j.jnucmat.2018.07.044>.
- [42] M. Kiritani, Radiation rate dependence of microstructure evolution, *J. Nucl. Mater.* 169 (1989) 89–94, [https://doi.org/10.1016/0022-3115\(89\)90524-2](https://doi.org/10.1016/0022-3115(89)90524-2).
- [43] T. Okita, T. Kamada, N. Sekimura, Effects of dose rate on microstructural evolution and swelling in austenitic steels under irradiation, *J. Nucl. Mater.* 283–287 (2000) 220–223, [https://doi.org/10.1016/S0022-3115\(00\)00355-X](https://doi.org/10.1016/S0022-3115(00)00355-X).

- [45] T. Okita, T. Sato, N. Sekimura, F.A. Garner, L.R. Greenwood, The primary origin of dose rate effects on microstructural evolution of austenitic alloys during neutron irradiation, *J. Nucl. Mater.* 307–311 (2002) 322–326, [https://doi.org/10.1016/S0022-3115\(02\)01202-3](https://doi.org/10.1016/S0022-3115(02)01202-3).
- [46] F. de la Peña, V.T. Fauske, P. Burdet, E. Prestat, P. Jokubauskas, M. Nord, T. Ostasevicius, K.E. MacArthur, M. Sarahan, D.N. Johnstone, J. Taillon, A. Eljarrat, V. Migunov, J. Caron, T. Furnival, S. Mazzucco, T. Aarholt, M. Walls, T. Slater, F. Winkler, B. Martineau, G. Donval, R. McLeod, E.R. Hoglund, I. Alxneit, I. Hjorth, T. Henninen, L.F. Zagonel, A. Garmannslund, A. Skorikov, Hyperspy/hyperspy v1.4.1, doi:10.5281/zenodo.1469364.
- [47] E.A. Kenik, *Irradiation-induced Microstructural Changes in Alloy X-750*, Microsc. Microanal., Cleveland, OH, 1997.
- [48] L.R. Greenwood, D.W. Kneff, R.P. Skowronski, F.M. Mann, A comparison of measured and calculated helium production in nickel using newly evaluated neutron cross sections for ^{59}Ni , *J. Nucl. Mater.* 123 (1984) 1002–1010, [https://doi.org/10.1016/0022-3115\(84\)90209-5](https://doi.org/10.1016/0022-3115(84)90209-5).
- [49] R.S. Nelson, J.A. Hudson, D.J. Mazey, The stability of precipitates in an irradiation environment, *J. Nucl. Mater.* 44 (1972) 318–330, [https://doi.org/10.1016/0022-3115\(72\)90043-8](https://doi.org/10.1016/0022-3115(72)90043-8).
- [50] H.J. Frost, K.C. Russell, Recoil resolution and particle stability under irradiation, *J. Nucl. Mater.* 104 (1981) 1427–1432, [https://doi.org/10.1016/0022-3115\(82\)90800-5](https://doi.org/10.1016/0022-3115(82)90800-5).
- [51] R.S. Averback, P. Bellon, *Fundamental Concepts of Ion-Beam Processing*, in: *Mater. Sci. With Ion Beams*, Springer, 2009, pp. 1–28, https://doi.org/10.1007/978-3-540-88789-8_1.